Supplementary Information (SI) for Nanoscale.

Exploring Spin Multiplicity in MoS_2

Sudipta Khamrui,[†] Kamini Bharti,[†] Daniella Goldfarb,[‡] Tilak Das,[*,†] and Debamalya Banerjee[*,†]

†*Department of Physics, Indian Institute of Technology Kharagpur, Kharagpur, 721302, India.*

‡*Department of Chemical and Biological Physics, Weizmann Institute of Science, Rehovot, 76100, Israel.*

E-mail: tilak.das@phy.iitkgp.ac.in; debamalya@phy.iitkgp.ac.in

Analysis of the MoS_2 nanoparticle phase formation

To understand the sample matrix, we synthesized two more batches of MoS_2 samples at the temperatures of 170°C and 230°C with the molar ratio of 1:2, and we named them as sample B0 and B1. Figure S1b shows the XRD spectrum of the samples, where it can be seen that the samples synthesised at 200°C and 230°C showed prominent 2H-MoS_2 phase. However, the disulfide crystalline nature became very weak for the sample synthesised at 170°C. Apart from that there is a broad line shape in between 20° - 30°. By comparing the XRD spectra with that of hydrothermally treated MoO_3 (MoO_3 powder was dissolved in 35 ml dl water and kept in the autoclave at 200°C for 24 hr), it can be said that this broad line shape appears due to incomplete sulfurization of MoO_3.

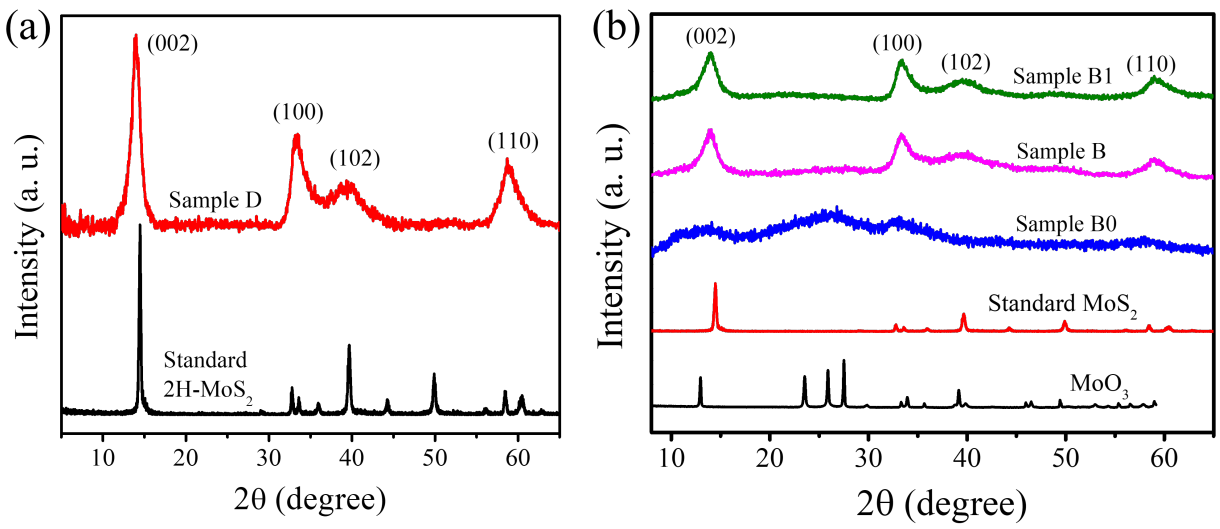

Figure S1: (a) A comparison in XRD spectra between the as-synthesised sample-D and the commercially procured 2H-MoS_2 sample (Source: Sigma Aldrich, India). (b) XRD spectra of sample B1 (synthesised at 230°C), sample B (synthesised at 200°C) and sample B0 (synthesised at 170°C). A comparison of the phase formation has been presented with respect to standard 2H-MoS_2 and hydrothermally treated MoO_3.

Understanding of the sample matrix though XPS measurements

Next, we performed XPS measurements to probe the evolution in chemical bonds with synthesis temperature as shown in Figure S2. It can be seen that three kinds of oxidation states for Mo-atom are present (Mo^{4+}, Mo^{5+} and Mo^{6+}) in Mo(3d) spectrum of sample B0.[1] The Mo^{4+} oxidation state appears from the Mo-S bonds of MoS_2. The Mo^{6+} doublets come from the unreacted Mo-O bonds of MoO_3, whereas the Mo^{5+} doublets appear from the oxygen vacancy rich MoO_{3-x} content. The presence of oxygen vacancies has also been verified from the CW-EPR measurements. With increasing reaction temperature, the contribution from unreacted MoO_3 decreased. Instead, the unreacted oxide resides in the form of reduced phase (MoO_{3-x}), which agrees with the EPR measurements of all the as-synthesised samples.

By analysing the S(2p) spectra, we can identify two kinds of S^{2-} oxidation state and a doublet appearing from S-O bonds. The presence of the S-O doublet indicates to the

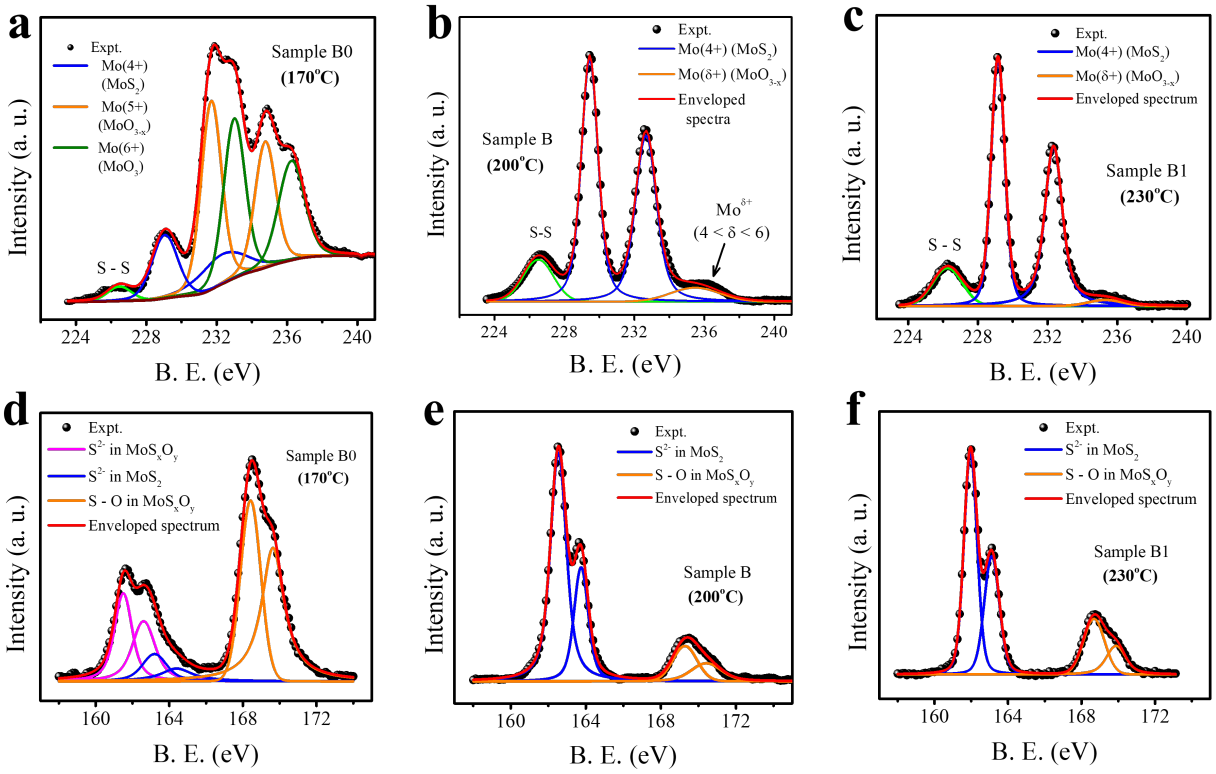

Figure S2: Chemical state evolution of MoS_2 with varying synthesis temperature. (a-c) Mo(3d) XPS spectra of the MoS_2 samples synthesised at the temperatures of 170°C (sample B0), 200°C (sample B) and 230°C (sample B1) with 1:2 molar ratio. (d-f) S(2p) XPS spectra of the same.

existence of Mo-S-O or Mo-O-S type bonds, whereas the first S^{2-} doublet indicates to the presence of mixed environment S^{2-} ions (S-Mo-O type bonds in MoS_xO_y).[2,3] As there are possibilities of both Mo-S-O or Mo-O-S type bonds and it is difficult to distinguish between them, we can generally say that there is a certain amount of oxidised molybdenum sulfide in the form of MoS_xO_y.

From study of structural and chemical bonds evolution with the varying growth temper-

ature, the following reaction pathway can be visualised[4]

$$CH_4N_2S + H_2O \rightarrow NH_3 + H_2S + CO_2 \tag{1}$$

$$H_2S + OH^- \rightarrow S^{2-}$$

$$MoO_3 + S^{2-} \rightarrow MoO_{3-x}S_x \ or \ Mo(SO_4) \rightarrow MoO_{3-x} + MoS_2 + S$$

Considering the above discussed structural and chemical bond information, we can say that our synthesised samples posses mixed phases of MoS_2, MoO_{3-x} and MoS_xO_y. Although, it is difficult to establish whether the sample is a composite like MoS_2 + MoO_{3-x} or the interconnected matrix like MoS_2-MoO_{3-x}. Still by considering the high pressure reaction condition in hydrothermal method and the presence of MoS_xO_y, we can assume that there are plenty of MoO_{3-x} regions in the samples which are interconnected with MoS_2 matrix through MoS_xO_y regions.

HR-STEM image of sample D

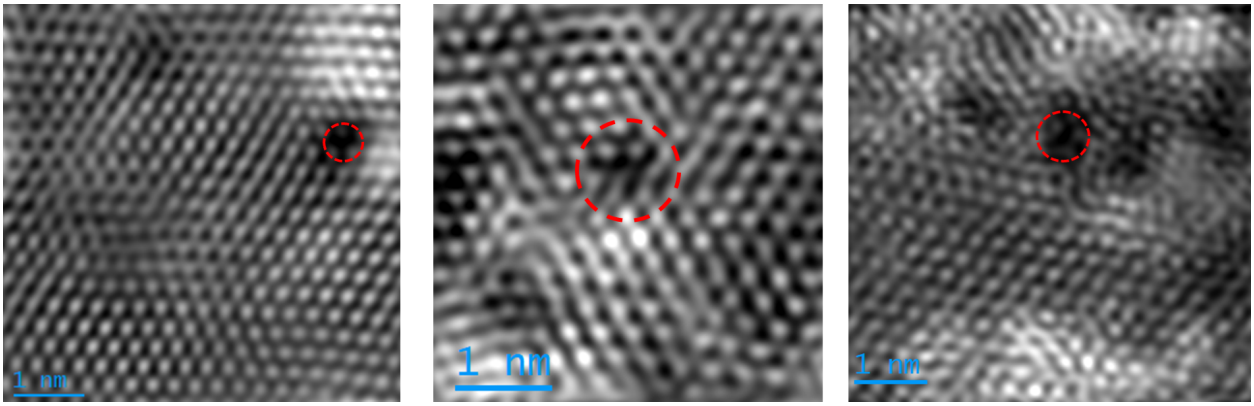

Figure S3: ADF-STEM images of sample D measured at different location on 300 mesh holey carbon grid. Red dotted circles mark the positions of defect sites.

ADF-STEM measurements were carried out to probe the defects of our synthesised 2H-MoS_{2-x} nanocrystals microscopically. **Figure S3** shows the STEM images of sample D measured at different positions on holey carbon grid. Few sulfur atoms are missing at the marked atomic sites, which seem to form sulfur vacancy defects. Due to the multilayer nature of the 2H-MoS_{2-x} nanocrystals, it was difficult to get a good focus and resolution during measurements.

EPR spectra simulation parameters

Table S1: List of the EasySpin simulation parameters for sample A, B, C, D, E and C1. A voigtian lineshape broadening was considered for the simulation. Line width broadening values are written in the third bracket for each peak. The first value represents the Gaussian broadening, while the second one gives the Lorentzian contribution. The ZFS parameters are written within a third bracket.

Sample	V1 (spin = 3/2)	V2 (spin = 3/2)	V3 (spin = 1/2)
A	$g_x = g_y = g_z = 2.065$ g_{strain} = (0.07 0.07 0.07) weight = 18 % lwpp = [5.5 2.0] mT [$\mathcal{D}$ $\mathcal{E}$] = [320 30] MHz	$g_x = 2.036$ $g_y = 2.000$ $g_z = 1.980$ g_{strain} = (0.06 0.00 0.00) weight = 30 % lwpp = [3 2] mT [$\mathcal{D}$ $\mathcal{E}$] = [80 20] MHz	$g_x = g_y = 1.934$ $g_z = 1.892$ g_{strain} = (0.0 0.00 0.02) weight = 52 % lwpp = [1.0, 1.5] mT
B	$g_x = g_y = g_z = 2.065$ g_{strain} = (0.07 0.07 0.07) weight = 14 % lwpp = [5.5 2.0] mT [$\mathcal{D}$ $\mathcal{E}$] = [320 30] MHz	$g_x = 2.036$ $g_y = 2.000$ $g_z = 1.984$ g_{strain} = (0.07 0.00 0.00) weight = 51 % lwpp = [3 2] mT [$\mathcal{D}$ $\mathcal{E}$] = [80 20] MHz	$g_x = g_y = 1.934$ $g_z = 1.890$ g_{strain} = (0.0 0.00 0.02) weight = 35 % lwpp = [1.2 1.2] mT
C	$g_x = g_y = g_z = 2.062$ g_{strain} = (0.07 0.07 0.07) weight = 17 % lwpp = [5.5 2.0] mT [$\mathcal{D}$ $\mathcal{E}$] = [320 30] MHz	$g_x = 2.035$ $g_y = 2.000$ $g_z = 1.984$ g_{strain} = (0.07 0.00 0.00) weight = 51 % lwpp = [3.5 2] mT [$\mathcal{D}$ $\mathcal{E}$] = [80 20] MHz	$g_x = g_y = 1.934$ $g_z = 1.890$ g_{strain} = (0.0 0.00 0.03) weight = 32 % lwpp = [1.5 1.2] mT
D	$g_x = g_y = g_z = 2.065$ g_{strain} = (0.07 0.07 0.07) weight = 18 % lwpp = [5.5 2.0] mT [$\mathcal{D}$ $\mathcal{E}$] = [320 30] MHz	$g_x = 2.045$ $g_y = 2.000$ $g_z = 1.984$ g_{strain} = (0.06 0.00 0.00) weight = 60 % lwpp = [3 2] mT [$\mathcal{D}$ $\mathcal{E}$] = [80 20] MHz	$g_x = g_y = 1.934$ $g_z = 1.890$ g_{strain} = (0.0 0.00 0.02) weight = 22 % lwpp = [1.6 1.2] mT

Table S1 *(Continued.)*

E	$g_x = g_y = g_z = 2.060$ g_{strain} = (0.08 0.08 0.08) weight = 43 % lwpp = [5.5 2.5] mT [$\mathcal{D}$ $\mathcal{E}$] = [320 30] MHz	$g_x = 2.045$ $g_y = 2.002$ $g_z = 1.984$ g_{strain} = (0.07 0.00 0.00) weight = 34 % lwpp = [2.5 1.0] mT [$\mathcal{D}$ $\mathcal{E}$] = [80 20] MHz	$g_x = g_y = 1.928$ $g_z = 1.882$ g_{strain} = (0.0 0.00 0.01) weight = 23 % lwpp = [2.2 1.3] mT
C1	$g_x = g_y = g_z = 2.060$ g_{strain} = (0.08 0.08 0.08) weight = 8 % lwpp = [5.5 2.0] mT [$\mathcal{D}$ $\mathcal{E}$] = [320 30] MHz	$g_x = 2.024$ $g_y = 1.995$ $g_z = 1.966$ g_{strain} = (0.025 0.000 0.020) weight = 92 % lwpp = [1.5 1.4] mT [$\mathcal{D}$ $\mathcal{E}$] = [180 58] MHz	- -

The zero field splitting (ZFS) parameters were taken equal in the simulation of all the as-synthesised samples ($\mathcal{D}$ = 320 MHz, $\mathcal{E}$ = 30 MHz for V1; $\mathcal{D}$ = 80 MHz, $\mathcal{E}$ = 20 MHz for V2). However, the ZFS of sample C1 adapted almost a three times higher value as compared to sample C to match the fine structures of the EPR lineshape for sample C1 ($\mathcal{D}$ = 180 MHz, $\mathcal{E}$ = 58 MHz for V2). This increment in ZFS value may be due to the change in the local structure of MoS_2 around V2 centre in the enhanced crystalline phase.

Effect of synthesis temperature on the defect centres probed by CW-EPR measurements

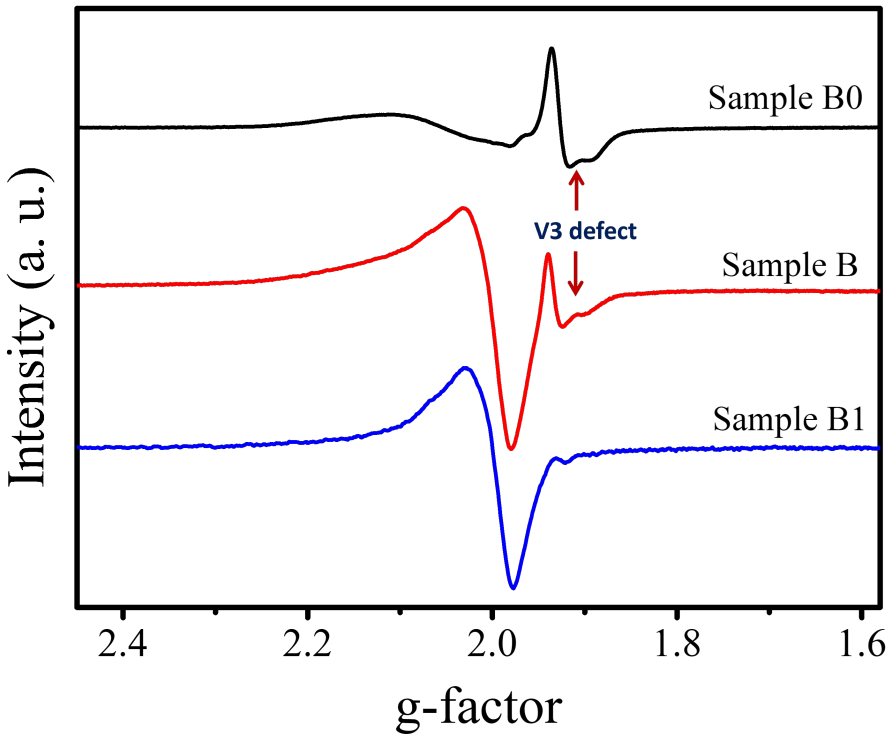

Figure S4: X-band CW-EPR measurements of sample B0, B and B1 synthesised at 170°C, 200°C and 230°C, respectively. All of these EPR measurements were carried out at 20K. The x-axis was converted in g-scale instead of magnetic field for direct comparison of the g-values of EPR signals.

X-band CW-EPR measurements were carried out at 20K to probe the evolution of defects with synthesis temperature. Figure S4 shows the CW-EPR spectra of the samples synthesised at 170°C, 200°C and 230°C, respectively. It can be seen that the contribution of V3 defect gradually decreases with increasing synthesis temperature. Moreover, the axial symmetry of V3 centre is clearly seen in EPR measurement of sample B0, which has been identified as oxygen vacancy of MoO_{3-y} phase in the main text.

Echo detected field sweep measurements in X- and W-band

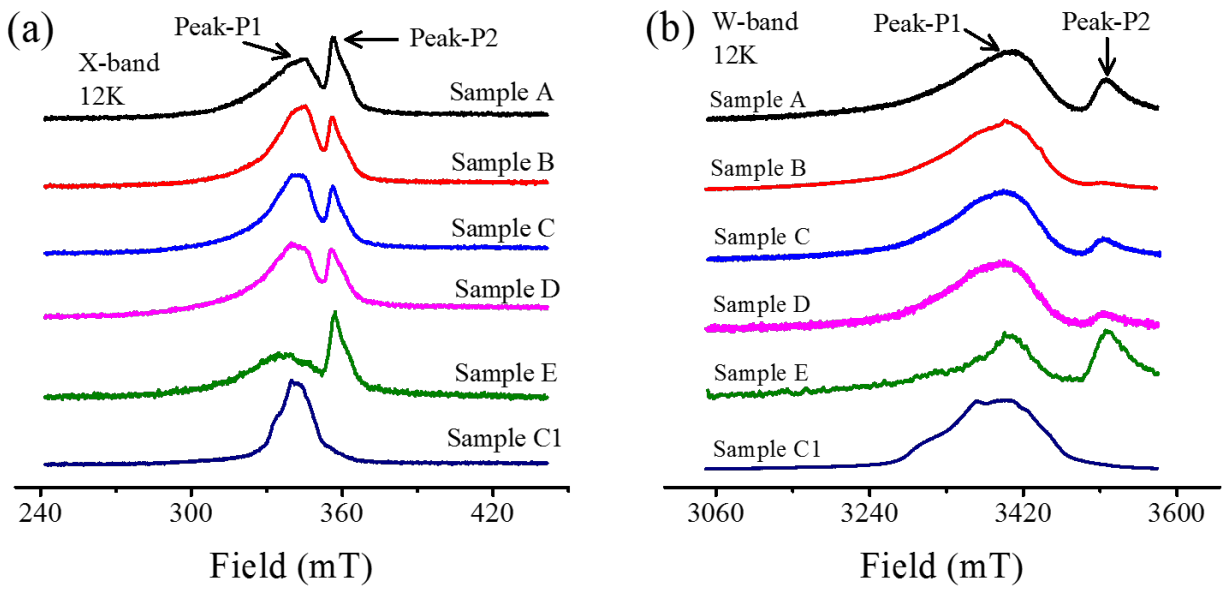

Figure S5: (a) X-band echo detected field sweep measurements at 12K. (b) The same in W-band.

A 10 ns - 130 ns - 20 ns pulse sequence was used and the integrated echo intensity was measured with the variation in external magnetic field through 2-step phase cycling program. Both the X- and W-band echo detected field sweep measurements were performed at 12K temperature and shown in Figure S5.

Pulse sequence for Inversion Recovery measurements

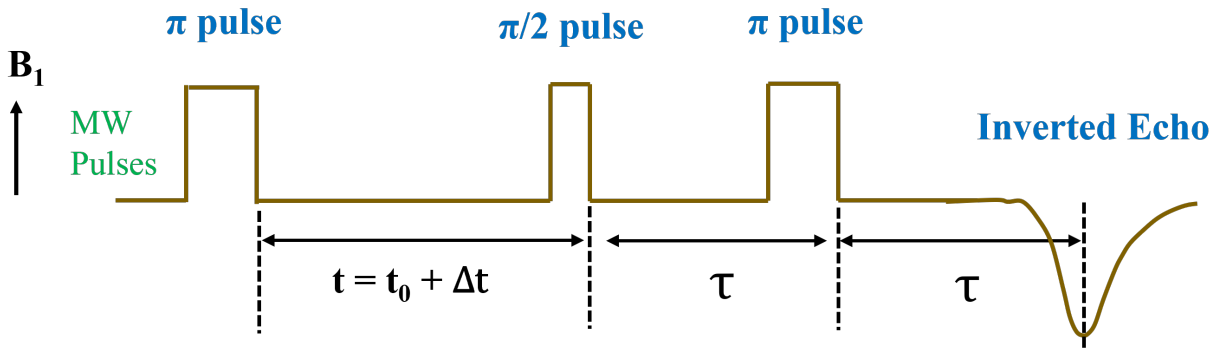

Figure S6: Sequence of the microwave pulses applied for inversion recovery experiment. A 10 ns microwave pulse was used as $\pi/2$ pulse. The inter-pulse separation time was set at 130 ns, while initial separation between the inversion and detection pulses was set at 300 ns.

All of the microwave pulses were applied from the $+x$ channel. A 20 ns π pulse was applied at t = 0 ns as the inversion pulse. The separation between the inversion and detection pulses was incremented by 10 μs and the integrated echo intensity was monitored. The echo intensity was recorded through 2 step phase cycling program to avoid the artefact signals in the measurements.

Spin-lattice relaxation measurements in X- and W-band

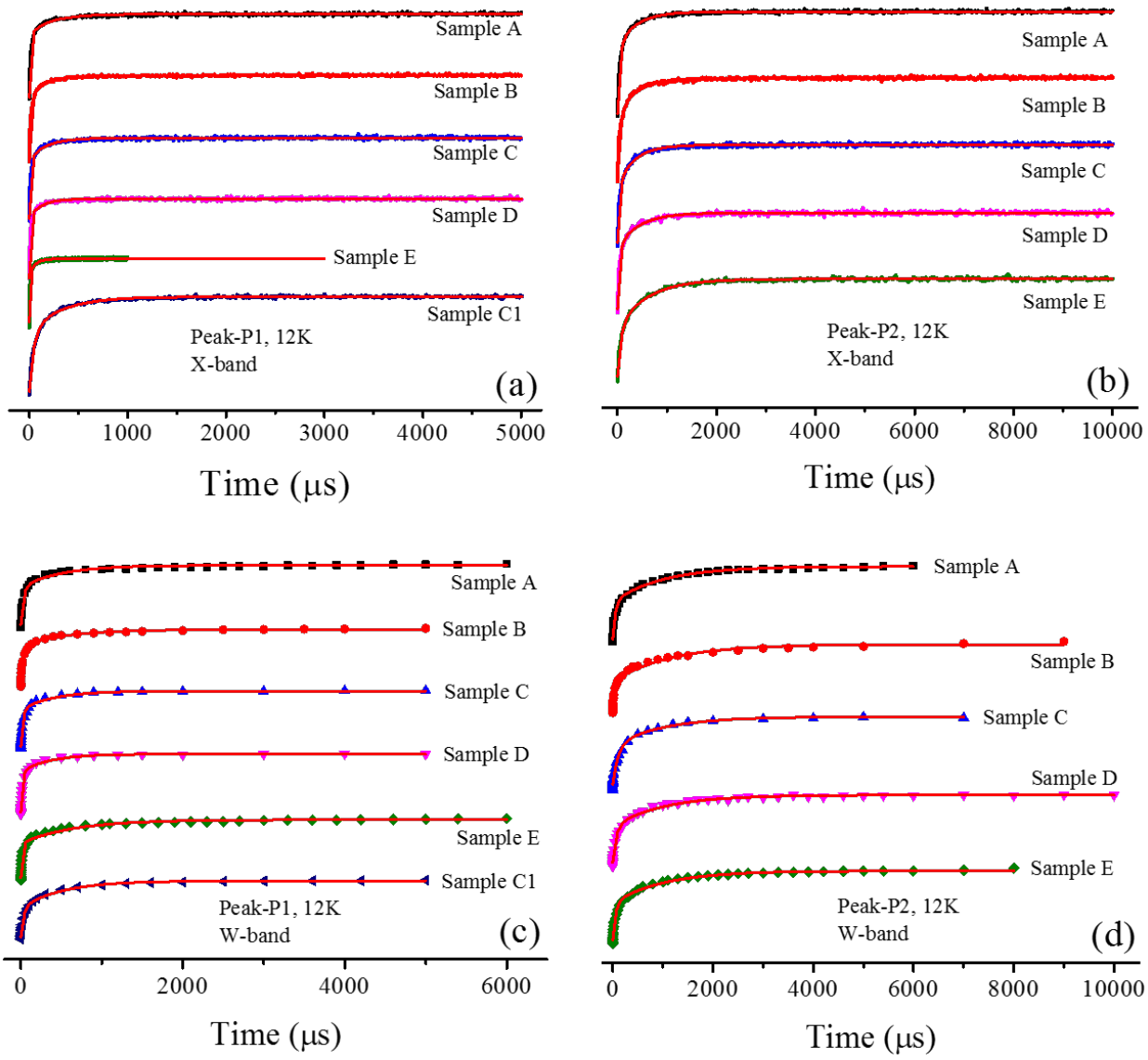

Figure S7: (a, b) Spin-lattice relaxation measurements at the position of Peak-P1 and Peak-P2 at 12K in X-band. (c, d) The same in W-band. All measurements were carried out with 2-step phase cycling program.

Temperature dependent spin-lattice relaxation measurements

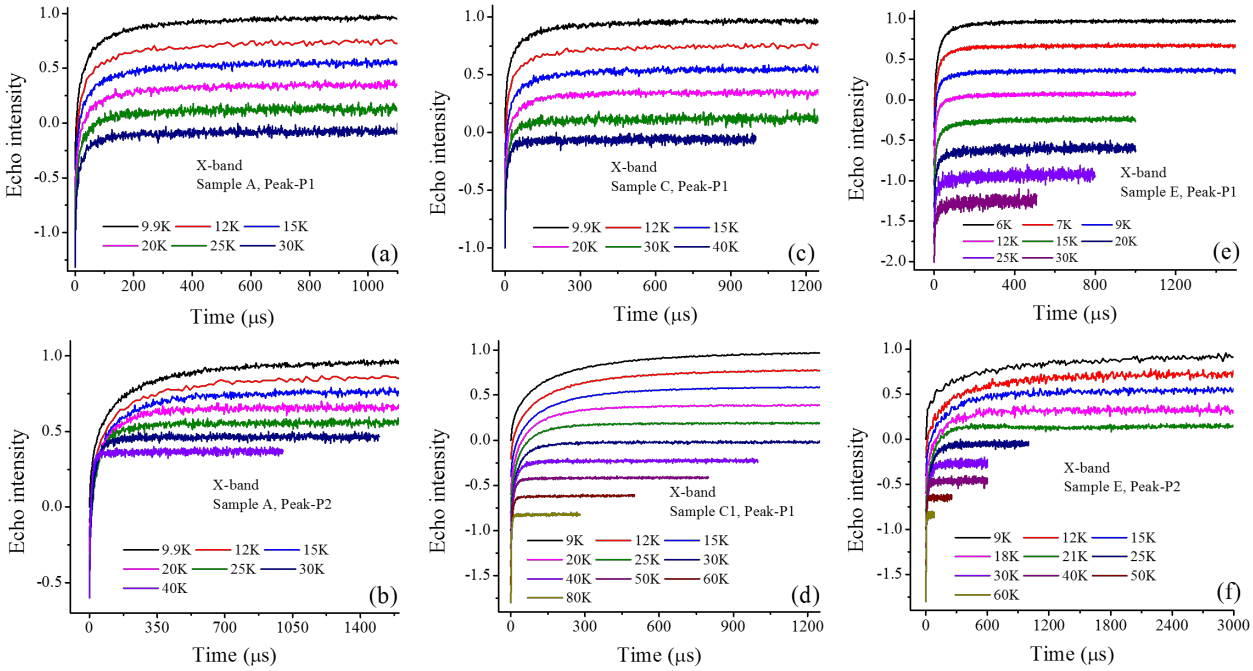

Figure S8: X-band temperature dependent inversion recovery measurements.

ELDOR Detected NMR Measurements

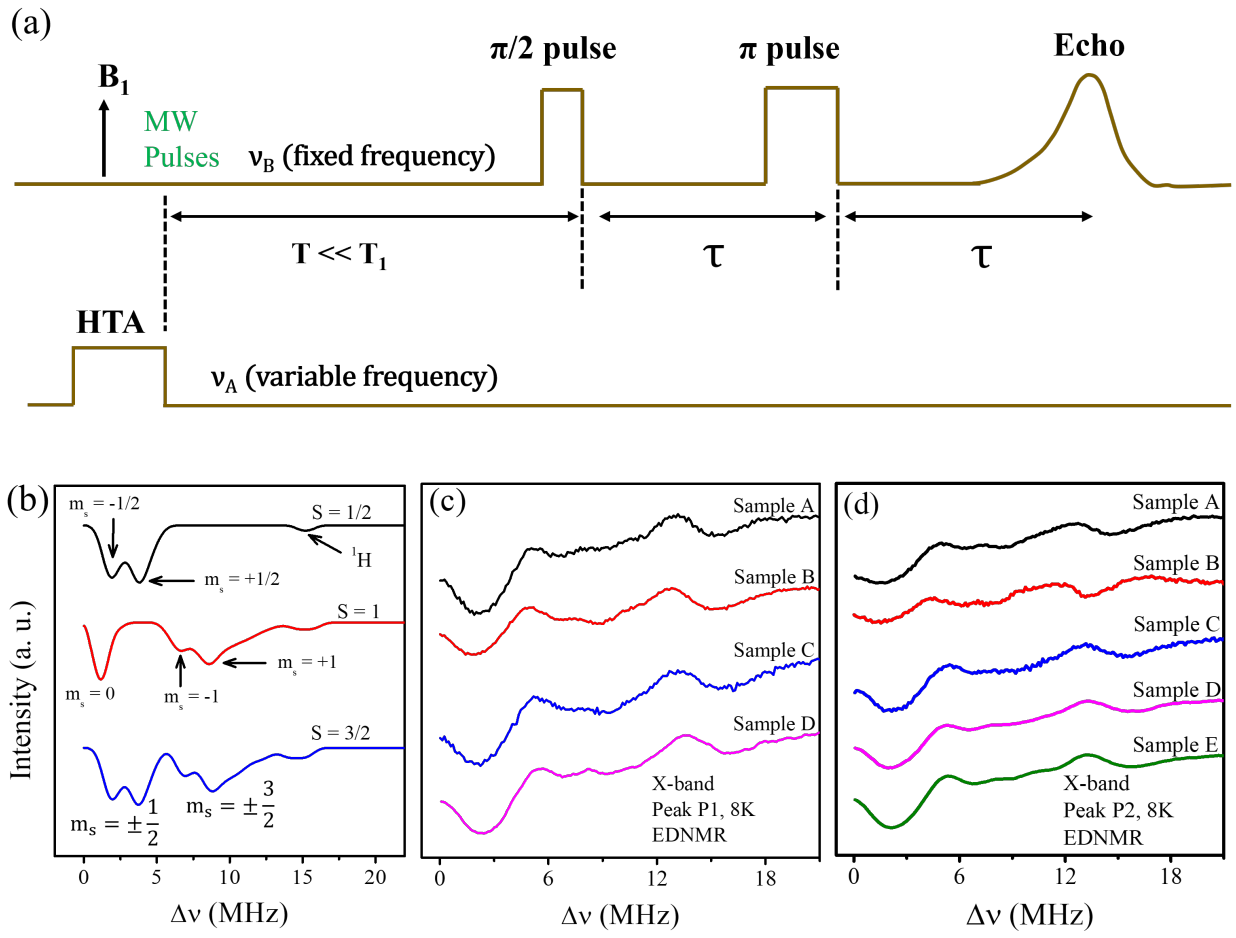

Figure S9: (a) X-band ELDOR detected NMR pulse sequence. HTA pulse (2000 ns) was given from ELDOR channel and the detection pulses were given from +x channel. (b) Simulated nuclear transitions of peak P1 in the X-band frequency. NMR transitions of different m_s manifolds are marked. (c) ELDOR detected NMR measurements of sample A, B, C, D and E at the position of Peak-P1. (d) The same for Peak-P2. A 50 ns ($\frac{\pi}{2}$) - 160 ns (τ) - 100 ns (π) detection pulse sequence was used in these measurements.

In this experiment the high turning angle (HTA) pulse is called the pump pulse whose frequency (ν_A) is continuously varied around the probe pulse frequency (ν_B). As the the HTA pulse posses high power high turning angle pulse, it can excite all the forbidden and allowed EPR transitions. When ν_A matches matches with ν_B, an allowed EPR transition gets intensified. On the other hand, the previously forbidden EPR transition triggers under

the frequency sweep of HTA pulse which then relaxes through the one of the allowed EPR transition. It will result into the decrease in observed signal intensity generating a nuclear transition at the frequency of ν_A - ν_B.

We considered $S = \frac{1}{2}$, 1 and $\frac{3}{2}$ spin states coupled with ^{95}Mo and ^{1}H hyperfine active nuclei in the simulations. If we consider spin-$\frac{1}{2}$ centre, the broad feature in the range 6 - 12 MHz of EDNMR spectra, that originates from nuclear transitions of $m_s = \pm\frac{3}{2}$ manifold, is not reproduced in simulation, whereas considering spin-1, the low frequency EDNMR doublet (0 - 6 MHz), originating from nuclear transitions of $m_s = \pm\frac{1}{2}$ manifold, was absent. By comparing the simulated nuclear transitions with the experimental spectra, it can be safely said that both the V1 and V2 centres posses a spin state of $S = \frac{3}{2}$, where $m_s = \pm\frac{1}{2}$ doublet overlaps with one another with a moderate line broadening to form the broad lineshape in between 0 - 6 MHz and $m_s = \pm\frac{3}{2}$ doublet superimpose with one another to form the broad feature in between 6 - 12 MHz. In the simulation, we considered the following values of the hyperfine and quadrupole interactions:- $^{95}Mo : A_{hyperfine} = [5.0\ 5.0\ 8.0]\ MHz$, $Q_{quadrapole} = [-0.04\ -0.04\ +0.08]\ MHz$; and $^{1}H : A^{iso}_{hyperfine} = 0.55\ MHz$

HYSCORE Measurements

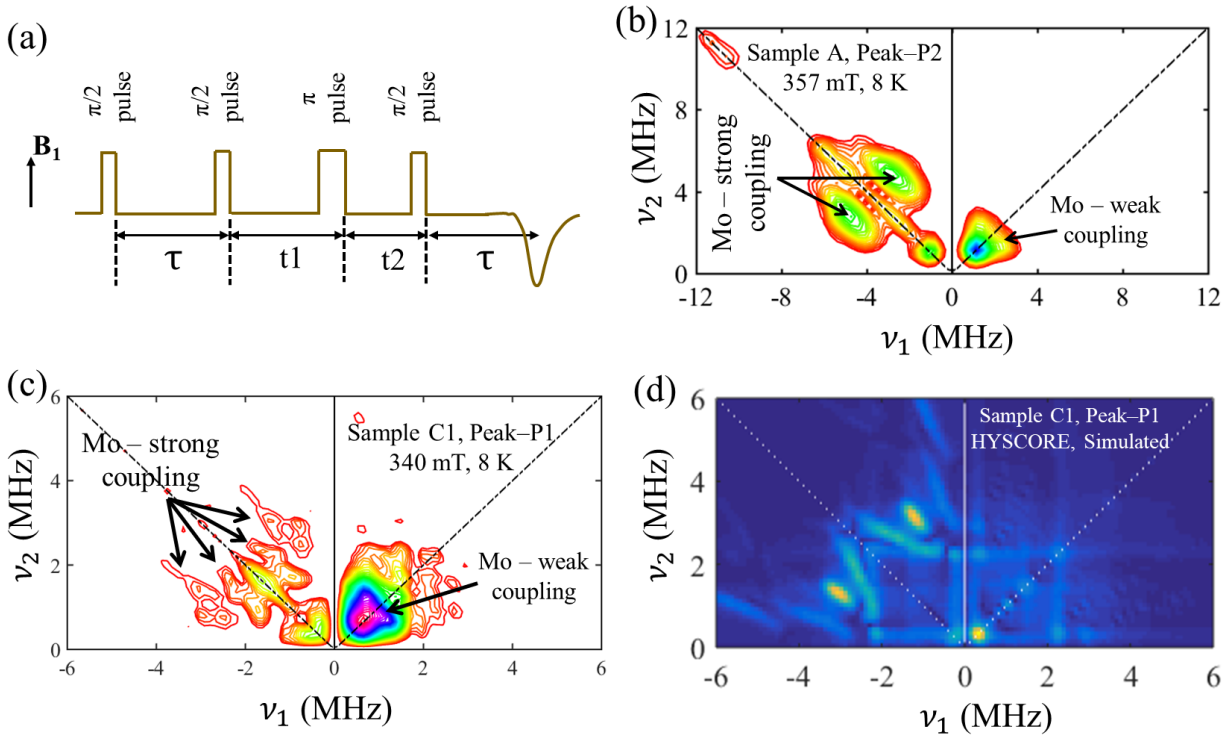

Figure S10: (a) Pulse sequence for X-band HYSCORE measurements. The measurements were carried out with 4-step phase cycling, where τ was kept fixed at 120 ns. But t1 and t2 were varied from an initial value of 100 ns. A 10 ns pulse was used as $\pi/2$-pulse, whereas a 18 ns pulse was found to be optimized π pulse. (b, c) X-band HYSCORE spectra of sample A (at P2 position) and sample C1 (at Peak-P1 position) measured at 8K. Both the two samples show a ^{95}Mo strong hyperfine coupling and a ^{95}Mo weak hyperfine coupling coming from distant nuclei. (d) Simulated X-band HYSCORE spectrum of sample C1 measured at the position of peak P1.

We used the same hyperfine and quadrupole interaction parameters as used for EDNMR simulation to simulate the strong ^{95}Mo hyperfine coupling for peak P1. It can be seen that the intense cross peaks centred around (-2.24, +2.24)MHz nearly matches with the strong coupling features of sample C1 at P1. Apart from this intense cross peak, there are other hyperfine correlations appearing from several other m_s manifolds, which are not clearly seen in the experimental spectra and required more careful data acquisition.

Echo detected field sweep spectra of coal and $MnCl_2$

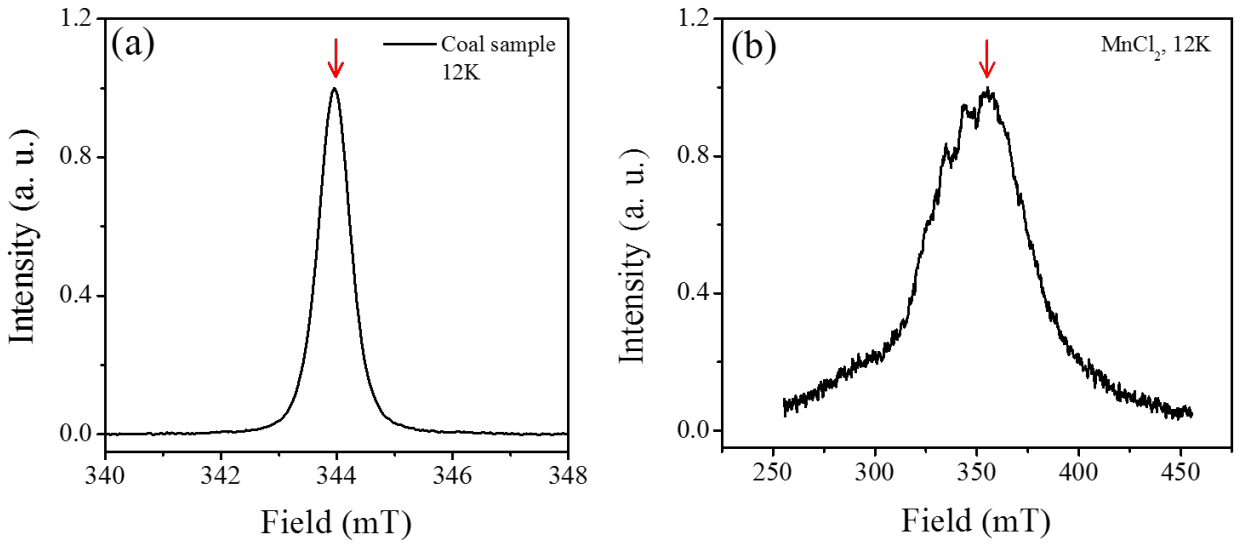

Figure S11: X-band echo detected field sweep spectra of coal sample (a) and $MnCl_2$ sample (b). Red vertical down arrow represents the field position where the nutation experiments were performed.

A Bruker standard coal sample was used as spin-$\frac{1}{2}$ source. A 0.8 mM solution of $MnCl_2$ was prepared in glycerol-water mixture for EPR measurement as a standard spin-$\frac{5}{2}$ source. Before inserting into the EPR cavity, the $MnCl_2$ sample was freeze quenched in liquid nitrogen.

Schematic of the pulse sequence for Rabi oscillation measurement

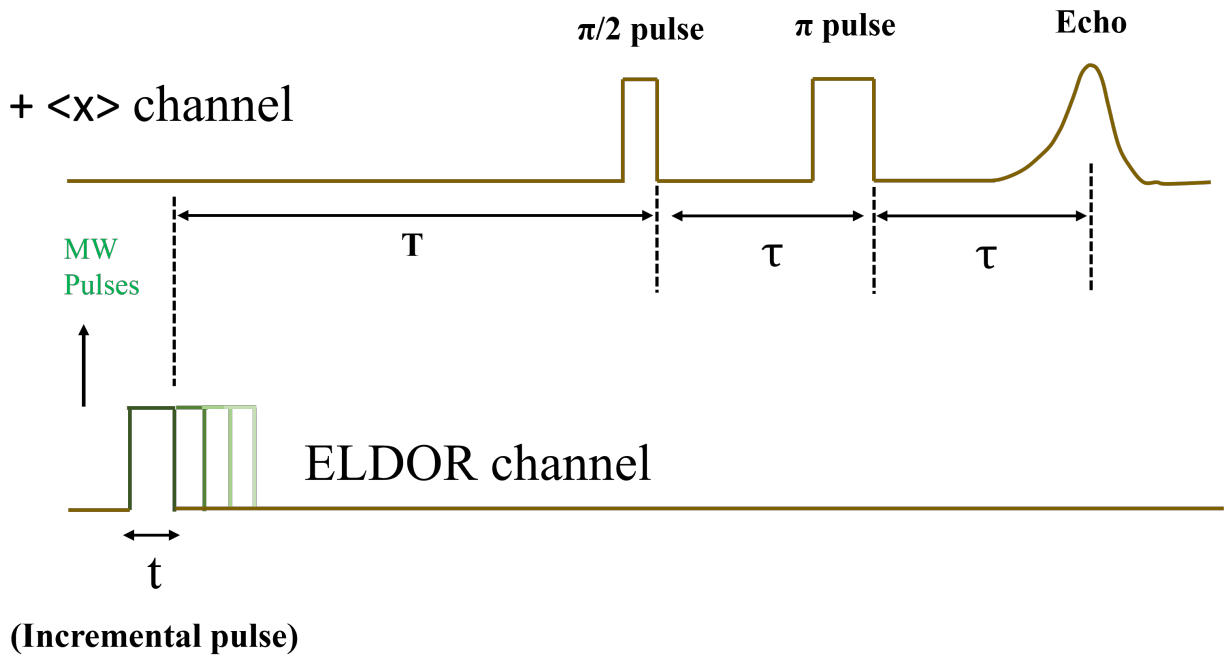

Figure S12: Rabi oscillation measurement pulse sequence. Value of T was set at 2 μs

The nutation pulse was applied from the ELDOR channel, while the detection pulses were applied from $+<x>$ MPFU channel. A 10 ns - 130 ns - 20 ns sequence was used as the detection pulse sequence. The nutation pulse length was incremented in the step of 2 ns and the integrated echo intensity was recorded with the nutation pulse length. For spin S, the nutation frequency of the transition between m_s to ($m_s \pm 1$) can be written as -

$$\omega_{m_s,m_s\pm1} = \omega_1\sqrt{S(S+1) - m_s(m_s \pm 1)} \tag{2}$$

where $\omega_1 = g\mu_B B_1/\hbar$ and B_1 is magnetic field of the microwave. From equation (1), it can be derived that the ratio of nutation frequency for spin-$\frac{5}{2}$, $\frac{3}{2}$ and $\frac{1}{2}$ will be $3:2:1$, respectively for the central transition ($m_s = -\frac{1}{2} \leftrightarrow \frac{1}{2}$).

Figure S13: A schematic diagram of few the prime defects centres models are presented

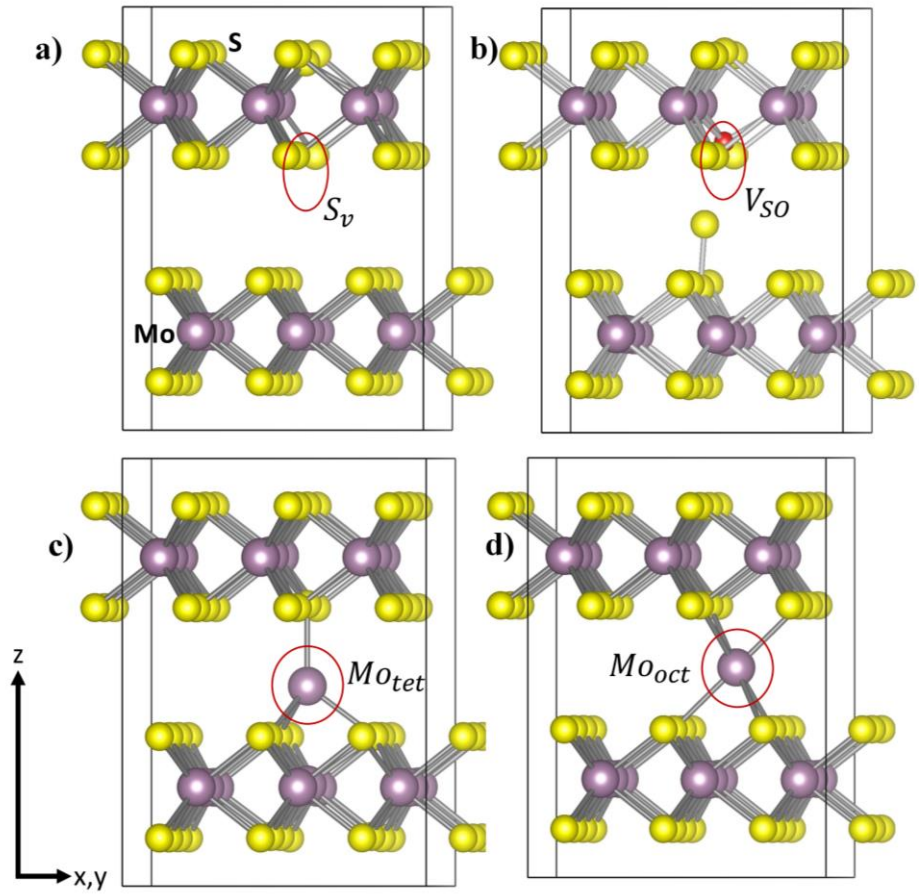

Figure S13: Only upon the strained conditions these three four charge centres (see below) are likely to be most relevant in the current exp. context as it is also consistent with other theoretical studies, while the other un-strained or uniaxially strained S_v or even with V_{SO} centres (oxygen atoms at S_v vacancy), these charge centres are invisible (no charge-localization) and it will be discussed briefly in this SI and nevertheless partially in the results section of the main manuscript. In a referential cartesian axis, a schematic presentation of the three native point-defects (red circles) within the given 3×3×1 supercell model of 2H-MoS_2, a sulphur vacancy red circle marked with S_v, and related Oxy-sulfide model, V_{SO}, in the top panels (a-b), and other two Mo interstitial sites marked with Mo_{tet} and Mo_{oct} in the given supercell model, Panels (b-c) respectively. Mo and S atoms are marked in the top left side panel only.

Figure S14: Calculated electronic band-gap of bulk 2H-MoS_2 with different set of Hubbard On-site effective U-values used for Mo(4d)

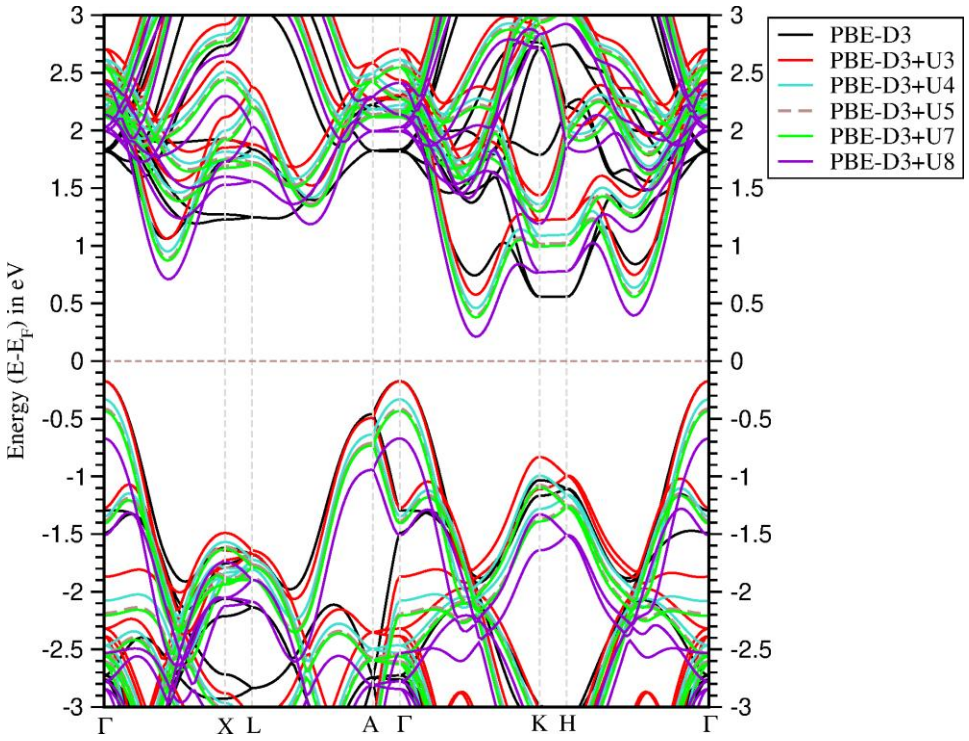

Figure S14: Calculated electronic band-gap from the full-Brillouin zone electronic band dispersion plots of bulk 2H-MoS_2 unit-cell with PBE-D3+U exchange-correlation functional in first-principles calculations with dispersion energy corrections at the D3-level. Different of effective U-values are used for Mo(4d), which varies from U3= 3 eV to U8 = 8 eV as labelled with different colour solid/dashed lines. Fermi level in each case is set to zero energy in eV.

Figure S15: Calculated electronic band-gap of bulk 2H-MoS_2 with different On-site Hubbard effective U-values used for both Mo(4d) and S(3p)

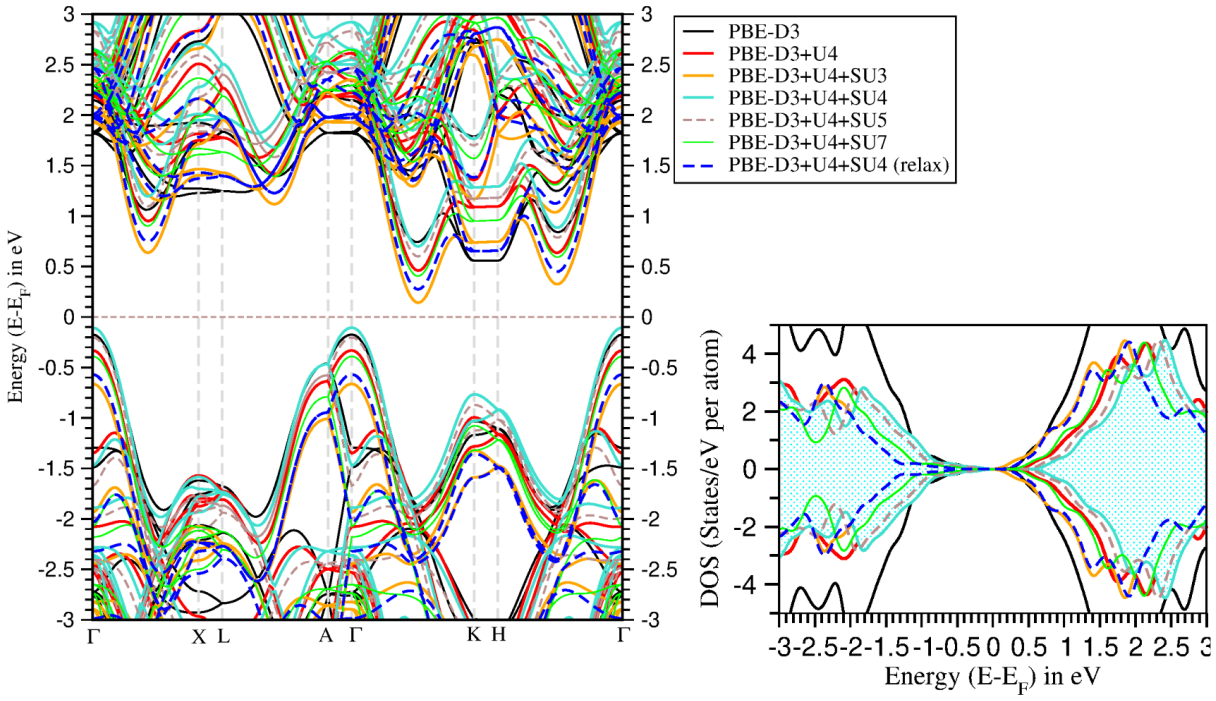

Figure S15: Calculated total electronic band structure (left) and total density of states (right bottom panel) of 2H-MoS2 bulk unit cell. Similar to the **Figure S16**, here fixed effective U_{Mo} (U4) = 4 eV is applied while U_S is varies from U3= 3 eV to U7 = 7 eV on the S-sublattices in the bulk 2H-MoS_2. Left side panel shown total electronic bands dispersion and right site panel show the corresponding total DOS data. Fermi level in each case is set to zero energy in eV.

Table S2: Calculated valence band top (VBT) and conduction band bottom (CBB) w.r.t. the Fermi level set to Zero

Table S2: Calculated valence band top (VBT) and conduction band bottom (CBB) w.r.t. the Fermi level set to Zero energy of the bulk 2H-MoS_2 as a function of the applied Hubbard onsite U on Mo(4d) and S(3p) orbitals in first-principles calculations using PBE-D3+U formulations are given. Here effective U values varies different from U3= 3.0 eV to U8= 8.0 eV on the Mo(4d) orbitals, while on the S-site (U_S) varies from the U = 3.0 eV to U7 = 7.0 eV at the given fixed U_{Mo} = 4.0 eV on the Mo(4d) sites. Indirect band gaps are measured as following the dispersion plot of the **Fig. S16** and **Fig. S17.** See methodology section in the main text for more details, respectively in the left- and right-side columns.

DFT Methods	**PBE-D3+U with only U_{Mo}(4d)**			**PBE-D3+U with U_{Mo}(4d) = 4.0 eV & U_S(3p)**		
	***VBT* in eV**	***CBB* in eV**	**Indirect Band gap (eV)**	***VBT* in eV**	***CBB* in eV**	**Indirect Band gap (eV)**
PBE-D3	-0.180	0.552	0.732	X	X	X
PBE-D3+U3 (U3 = 3.0 eV)	-0.181	0.567	0.748	-0.667	0.132	0.699
PBE-D3+U4 (U4 = 4.0 eV)	-0.336	-0.460	0.796	-0.110	0.699	0.809
PBE-D3+U5 (U5 = 5.0 eV)	-0.419	-0.401	0.820	-0.204	0.598	0.802
PBE-D3+U7 (U7 = 7.0 eV)	-0.438	0.377	0.815	-0.391	0.405	0.796
PBE-D3+U4 (U4 = 4.0 eV) [Full-relaxed]	X	X	X	-0.575	0.270	0.845

Table S3: Calculated defect formation energies of single sulphur vacancy (S_v) in the bulk 2H-MoS_2 crystal

Table S3: Calculated defect formation energies of single sulphur vacancy (S_v) in the bulk 2H-MoS_2 crystal, where choice of the different pseudo potentials (PAW or Ultrasoft) is tabulated in the current PBE-D3+U formulation of the chosen exchange-correlation functional (U_{Mo} = 4.0 eV on the Mo(4d) and U_S = 4.0 eV on the S(3p)). Impact of the exp. and first-principles cell volume relaxation is also tested and compared with the previously validated first-principles data[1-4]. See also **Figure S16** and **Fig. S17** and also **Table S1**.

Models/Parameters	**E_{form} (S_v) in eV/atom (PAW)**	**E_{form} (S_v) in eV/atom (USPP)**	**Indirect Band gap (eV) of Bulk 2H-MoS_2**
PBE-D3 (exp. Volume)	2.164	2.158	0.732
PBE-D3 (Full-relaxed Volume)	2.002	1.996	0.779
PBE-D3+U (Full-relaxed Volume)	2.164	2.180	0.845
Previous DFT data[1-4]	2.0-3.5 eV per atom		0.8-1.0 eV

1. Kapildeb Dolui, Ivan Rungger, Chaitanya Das Pemmaraju, and Stefano Sanvito, Possible doping strategies for MoS2 monolayers: An *ab initio* study, Phys. Rev. B **88**, 075420 (2013).
2. Yungang Zhou, Ping Yang, Haoyue Zu, Fei Gao, and Xiaotao Zu, *Phys. Chem. Chem. Phys.*, **15**, 10385 (2013).
3. Huiling Zheng et al., Tuning magnetism of monolayer MoS2 by doping vacancy and applying strain, Appl. Phys. Lett. 104, 132403 (2014).
4. Anne Marie Z. Tan, Christoph Freysoldt, and Richard G. Hennig, Stability of charged sulfur vacancies in 2D and bulk MoS2 from plane-wave density functional theory with electrostatic corrections, Phys. Rev. Mater. 4, 064004 (2020).

Figure S16: Calculated total and atom projected DOS of the S_v model of the unstrained 2H-MoS_{2-x}

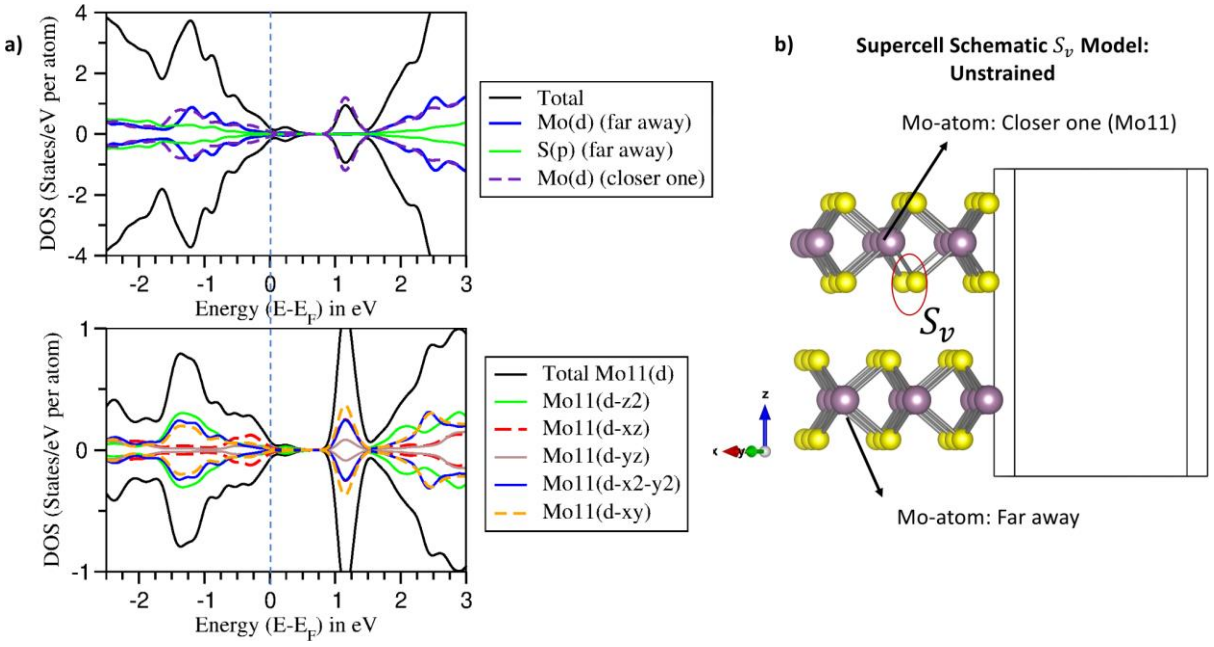

Figure S16: Calculated total and atom projected DOS of the S_v model of the unstrained 2H-MoS_{2-x}, using QE6.8 DFT code panel **a)**, and corresponding 3×3×1 supercell model as obtained from the atomic positions relaxation of the unstrained supercell marked with different atoms symbols and vacancy sites at panel **b)** as a result of the spin-density plots with a 3D IOS level 0.01 $e^-/Å^3$. A clean absence of the spin-density in the panel b) is associate with the empty pDOS seen in the DOS panel a) below the conduction bands.

Figure S17: Calculated total and atom projected DOS of the S_v model of the uni-axial strained 2H-MoS_{2-x}

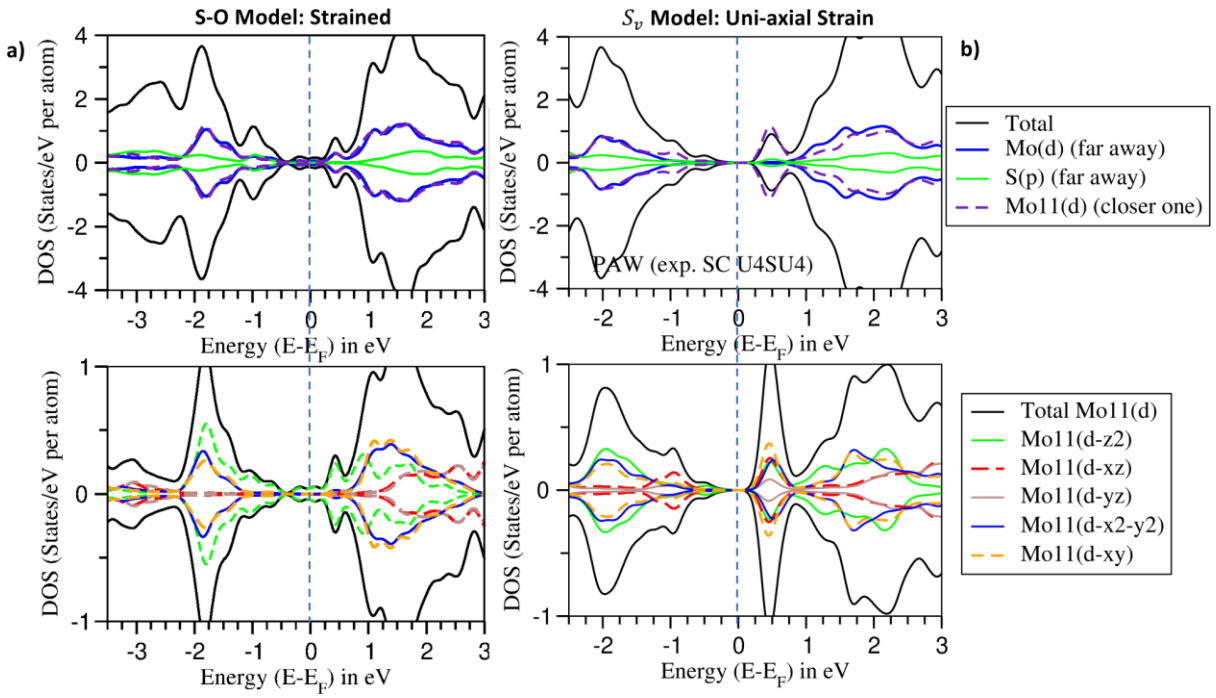

Figure S17: In the top left panels, calculated electronic DOS and pDOS of the Oxy-sulfide model at the S_v defect centre, panel **a)**, and uni-axial tensile strain on the pristine S_v defect models in panel **b)**. In either cases, the local Mo^{4+}-4d orbitals to the vacancy sites are projected (lower panels), and found no visible charge localization in S-deficit 2H-MoS_{2-x} models and consistent with pDOS plots.

Table S4: Calculated defect formation energies of single Mo interstitial Mo_{oct} and Mo_{tet} in the bulk 2H-MoS_2 crystal

Table S4: Calculated defect formation energies of single Mo interstitial (Mo_{oct} and Mo_{tet}) in the bulk 2H-MoS_2 crystal, where choice of current PBE-D3+U formulation of the chosen exchange-correlation functional (U_{Mo} = 4.0 eV on the Mo(4d) and U_S = 4.0 eV on the S(3p))

Models/Parameters	E_{form} (Mo_{oct}) in eV/atom	E_{form} (Mo_{tet}) in eV/atom	Indirect Band gap (eV) of Bulk 2H-MoS_{2-x}
PBE-D3+U	0.48	0.62	0.845 eV

Figure S18: Calculated electronic properties Mo interstitial at tetragonal sites (Mo_{tet}) in the host 2H-MoS_{2-x}

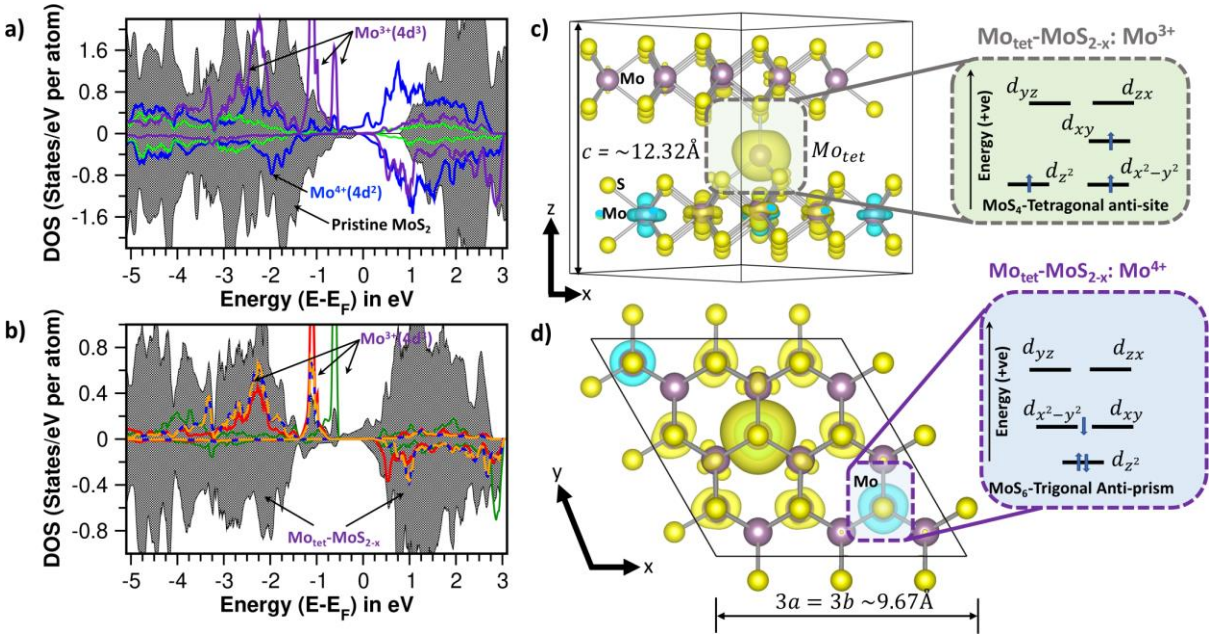

Figure S18: Calculated spin-centres from the single Mo interstitial (Mo_{tet}) at tetrahedral site in the nanocrystalline bulk phase of 2H-MoS_2 using current first-principles calculations. In the left panel **a)** majority and minority total density of states (DOS) of the pristine 2H-MoS_2, $Mo^{4+}(4d^2)$ and S(3p) projected DOS are shown with black shaded areas, blue solid lines, light green solids lines respectively, while the pDOS of the interstitial Mo_{tet} sites $Mo^{3+}(4d^3)$ is shown with the solid thick indigo color line. In the panel **b)** of the same $Mo^{3+}(4d^3)$ orbital decomposed DOS is shown where the total DOS of the Mo_{tet}-2H-MoS_{2-x} model is presented with black shaded area, and three other non-degenerate Mo-4d levels of Mo_{tet} are shown with color lines: Mo-d_{yz}/d_{xz} in red, Mo-d_{z2} in deep green and Mo-d_{xy}/d_{x2-y2} in orange/blue dashed or solid lines. Corresponding spin-density plots at the Mo_{tet} site (formal intermediate spin of $Mo(4d^3)$) and neighboring Mo-sites (formal $Mo^{3.5+}$ and hence weaker than intermediate spin-state of $Mo(4d^{2.5})$) with formal charge centers $Mo^{3+}(4d^3)$ and $Mo^{3.5+}(4d^{2.5})$ is shown, respectively and holds calculated spin-magnetic moment, 3.34 μ_B and 0.45 μ_B. These are plotted in the panels c) and d) around the single Mo_{tet} center with side and top views, those are calculated from the 54 atoms supercell of 2H-MoS_{2-x} model, with a 3D IOS level 0.01 $e^-/Å^3$ while a schematic sketch on their possible 4d-level occupancies is zoomed out at right side panels. Positive and negative spin-densities are in yellow and cyan color respectively.

Figure S19: Calculated Spin-properties S-vacancy and Mo interstitial at octahedral site (Mo_{tet}) of the 2D-Slab of host 2H-MoS_{2-x}

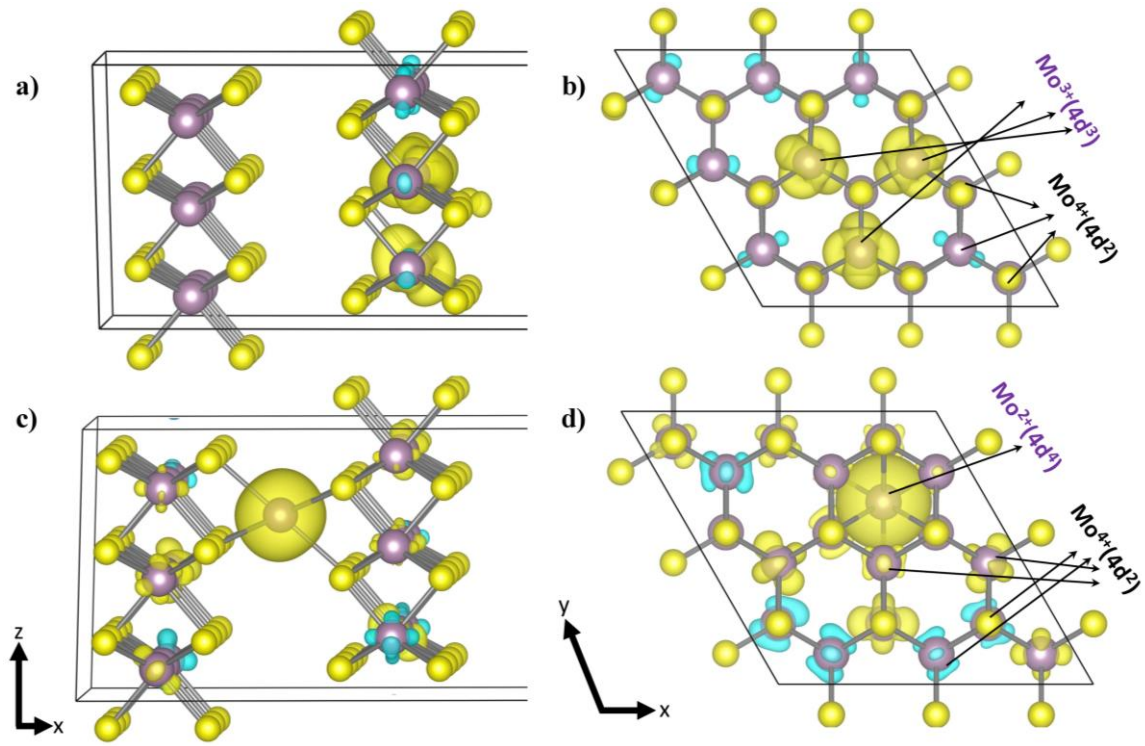

Figure S19: Calculated spin-density plots of the S-vacancy panel (a-b) and Mo_{oct} within the 2D slab model of the host 2H-MoS_{2-x} from first-principles calculations with side view (panel a and c) and top view (panel b and d). With a 3D IOS level 0.01 $e^-/Å^3$ these spin-densities are plotted.

Figure S20: Calculated electronic DOS properties of the S-vacancy (S_v) within the host 2H-MoS_{2-x}

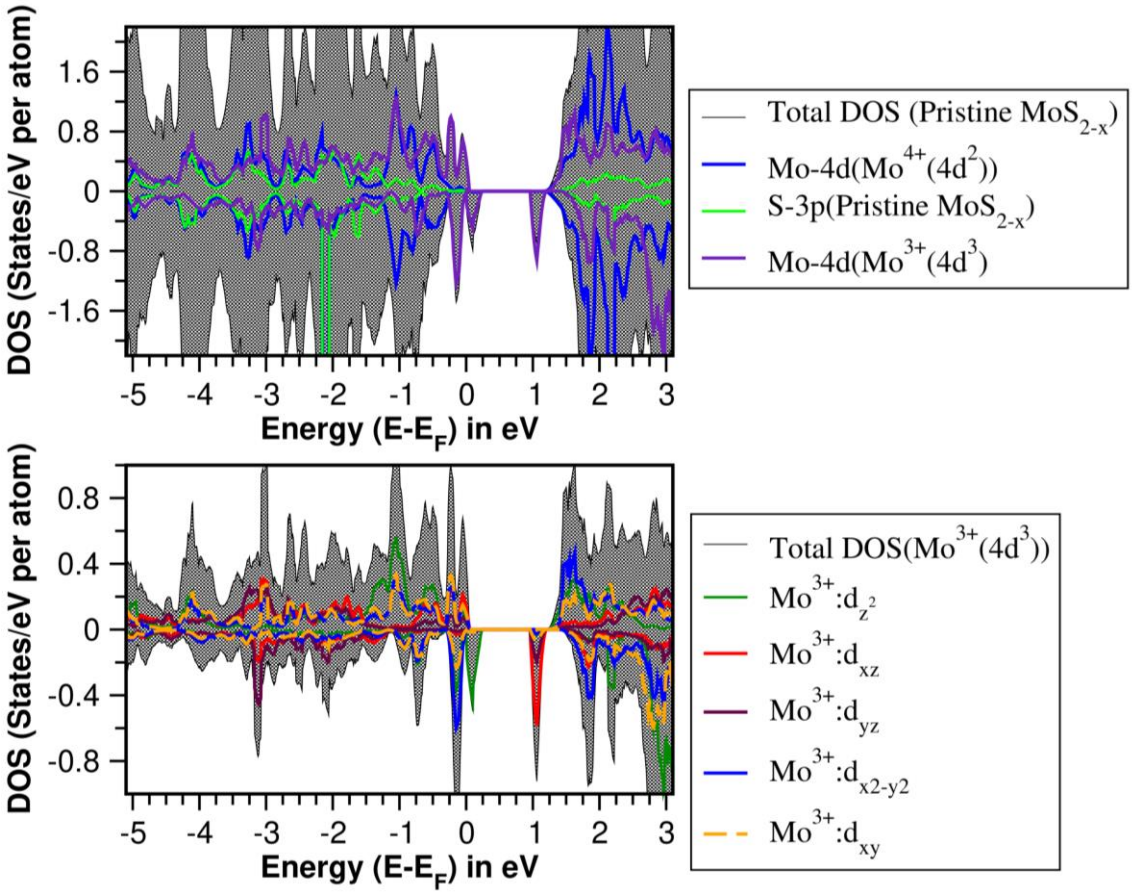

Figure S20: Calculated electronic density of states of the bulk S-deficit 2D slab of the 2H-MoS_{2-x} host lattice, and formal Mo^{4+}(4d) and S(3p) respectively in the top panel and orbital decomposed pDOS of the $Mo^{3+}(3d^3)$ is shown in the bottom panel. Color solid/dash lines are shown in the different panels, are labeled in the right-hand side boxes. Fermi level is set to zero of energy and the possible unpaired electron is located on the Mo-$4d_{z^2}$ of the $Mo^{3+}(4d^3)$ sub-lattice. Calculated spin-magnetic moment per Mo^{3+} sites are 1.39 μ_B.

Figure S21: Calculated electronic DOS properties of Mo-interstitial at the octahedral sites (*Mo_{oct}*) within the host 2H-MoS_{2-x}

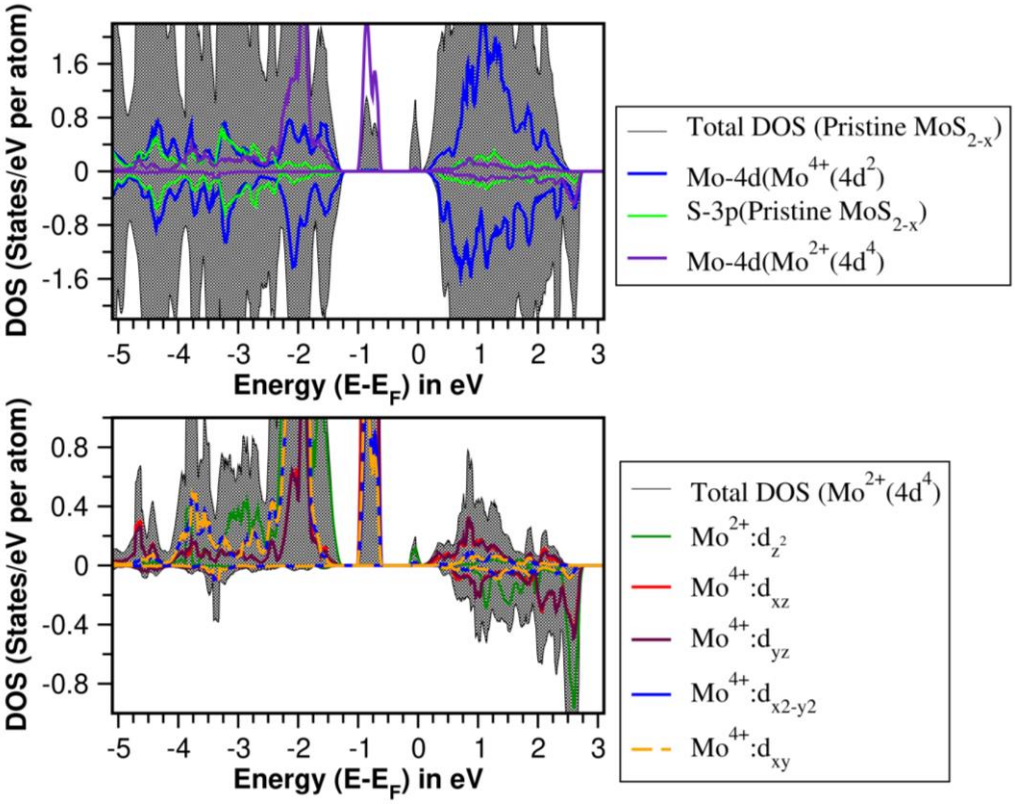

Figure S21: Calculated electronic density of states of the bulk S-deficit 2D slab of the 2H-MoS_{2-x} host lattice, and formal Mo^{4+}(4d) and S(3p) respectively in the top panel and orbital decomposed pDOS of the $Mo^{2+}(4d^4)$ is shown in the bottom panel. Color solid/dash lines are shown in the different panels, are labeled in the right-hand side boxes. Fermi level is set to zero of energy and the possible unpaired electron is located on the 3 degenerate Mo-$4d_{xy}$/$4d_{yz}$ /$4d_{xz}$ and one on the Mo-$4d_z^2$ of the $Mo^{2+}(4d^4)$ sub-lattice. Calculated spin-magnetic moment per Mo^{2+} sites are 3.9 μ_B.

DFT Modelling of Defects

Two major challenges have been mimicked through the approximated manner in the current DFT analysis of the point-defects at the moderate computational resource requirement and reasonable accuracy. First, the true nano-structure environment of the 2H-MoS_2, is modelled through the applied external strain on the bulk phase, because of the observed nano-particles size in the current exp. synthesis are comparable with bulk properties in 2D and found to be validated in our earlier work on quantum-confinement in layered dichalcogenides.[5] And secondly, the choice of the DFT exchange-correlation is set to PBE-D3+U formulation through the systematic search of the on-site Hubbard U either on Mo(4d) and or S(3p). The calculated data is bench marked with earlier single sulfur vacancy formation energies, S_v as reported from the higher level of post-DFT theory and modelling and also the use of the PBE-D3+U method is motivated from similar works on the layered oxides V_2O_5 and MoO_3 while one looks into the thermochemistry and electronic band gaps at the moderate computational loads.[6,7] These point defects in the current model of nano-structured 2H-MoS_2 is opted within a supercell of size 3×3×1, while the strain generated in the exp. synthesized sample was induced along with various external stimuli through in-plane tensile strain, i.e. 2.0%, 4.0%, 6.0% and a combined 6.0% in-plane and 4.0% out-of-plane tensile strain on the first-principles volume of the bulk 2H-MoS_2. The highest strain essentially correlated with observed exp. lattice parameter of the nano-structured 2H-MoS_2 in the current measurements, yielding values a = b = 3.161$\mathring{A}$ and c= 12.965$\mathring{A}$ (see also Table 1), compromising lattice value of 2H-MoS_{2-x} than the standard sample 2H-MoS_2. The single sulfur vacancy S_v formation energy (E_{form}) is estimated from the current first-principles theoretical calculations at absolute 0K with Eq. 3

$$E_{form}(S_v) = (E_{sv} - E_{pure} + \mu_s) \tag{3}$$

Where, E_{pure} is the total energy of the pure 2H-MoS_2 supercell without sulfur vacancy (pristine sample) and E_{Sv} is the total energy from the single S_v included 2H-MoS_2 supercell model and μ_S is the chemical potential of the sulfur at the Mo-rich/S-poor condition at the thermal equilibrium as defined with Eq. 4,

$$\mu_s = \frac{1}{2}\left(\mu_{MoS_2} - \mu_{Mo(bcc)}\right) \tag{4}$$

Here, μ_{MoS_2} is the total energy of the bulk 2H-MoS_2 unit cell and $\mu_{Mo(bcc)}$is the total energy of the known stable bcc cubic (body-centred cubic) unit cell of Mo, and the strategy has been well accepted in the earlier DFT studies and also values found remarkably well agreed with earlier DFT literature values performed at higher DFT Jacob's Laddar rung.[8,9] While for the other two defect with Mo_{tet} and Mo_{oct} the formation energy at the same footing of the current DFT formulation is estimated with the following Eq. 5,

$$E_{form}(Mo_{tet}\ or\ Mo_{oct}) = \left(E_{Mo} - E_{pure} - \frac{1}{2}\mu_{Mo(bcc)}\right) \tag{5}$$

Here E_{Mo} is the total energy of the 2H-MoS_2 bulk supercell containing the Mo intestinal defects (Mo_{tet} or Mo_{oct}) i.e. Mo atom is placed at the tetrahedral or octahedral site in the van der Waals spacing of the host lattice. A schematic diagram of these defect models is presented in the SI **Figure S13**.

Finally, we notice also the vacancy formation energies of the S_v at the given exchange-correlation with or without U term (see **Table S2** in SI), and found consistent result than earlier reported values, and proved the robustness of the current calculations strategy.[9,10] Nonetheless, the most demanding aspect of the applying U-term on the S-site is actually more interesting and would be disused for 3 major defect models, i.e. sulfur vacancies (S_v), Mo-interstitials (tetrahedral site, Mo_{tet} or octahedral site, Mo_{oct}) and Oxy-sulfides (V_{SO}) at the S_v centres.

Thus, in the current work, a systematic search of the on-site Hubbard U term on the Mo- and S sub-lattices are done while reference to their exp. band gap ($\sim$ 1.3 eV indirect) and expenses of S_v formation was tested systematically in the nano-structured 2H-MoS_2. In the SI **Figure S14 and Figure S15**, we have shown the calculated electronic band-edges position calculated using different Hubbard onsite-U values applied either on the Mo(4d) or on both Mo(4d) and S(3p) orbitals. The calculated band gap looks reasonable while one include Hubbard effective $U = 4$ eV both on the Mo(4d) and S(3p) with calculated indirect band gap at the DFT level 0.85 eV from the first-principles relaxed volume of 2H-MoS_2 bulk unit cell (see also SI **Table S2**). Compared to the exp. value, though this is about 35% lower band gap vs. exp. values, but better than than the standard DFT data 0.73 eV (about 50% underestimated).

Only, upon the strained conditions these three charge centres are likely to be most relevant in the current context as it is also consistent with the current exp. observation, while the other un-strained or uniaxial strained or even with V_{SO} centres (oxygen atoms at S_v vacancy), these charge centres are invisible and to be discussed briefly in main text. The calculated defect formation energies of the Mo-interstitial are presented in **Table S4** in the SI.

References

(1) Vasilopoulou, M.; Douvas, A. M.; Georgiadou, D. G.; Palilis, L. C.; Kennou, S.; Sygellou, L.; Soultati, A.; Kostis, I.; Papadimitropoulos, G.; Davazoglou, D.; others The influence of hydrogenation and oxygen vacancies on molybdenum oxides work function and gap states for application in organic optoelectronics. *Journal of the American Chemical Society* **2012**, *134*, 16178–16187.

(2) Dupin, J.-C.; Gonbeau, D.; Martin-Litas, I.; Vinatier, P.; Levasseur, A. Amorphous

oxysulfide thin films MOySz (M= W, Mo, Ti) XPS characterization: structural and electronic pecularities. *Applied surface science* **2001**, *173*, 140–150.

(3) Ryaboshapka, D.; Afanasiev, P. Molybdenum oxysulfide MoOS2 as a hydrogen evolution catalyst: On the possible role of coordinated oxygen. *Journal of Catalysis* **2023**, *426*, 30–38.

(4) Genuit, D.; Bezverkhyy, I.; Afanasiev, P. Solution preparation of the amorphous molybdenum oxysulfide MoOS2 and its use for catalysis. *Journal of Solid State Chemistry* **2005**, *178*, 2759–2765.

(5) Das, T.; Di Liberto, G.; Pacchioni, G. Quantum confinement in chalcogenides 2D nanostructures from first principles. *Journal of Physics: Condensed Matter* **2022**, *34*, 405301.

(6) Das, T.; Tosoni, S.; Pacchioni, G. Structural and electronic properties of bulk and ultrathin layers of V2O5 and MoO3. *Computational Materials Science* **2019**, *163*, 230–240.

(7) Das, T.; Tosoni, S.; Pacchioni, G. Layered oxides as cathode materials for beyond-Li batteries: A computational study of Ca and Al intercalation in bulk V2O5 and MoO3. *Computational Materials Science* **2021**, *191*, 110324.

(8) Dolui, K.; Rungger, I.; Pemmaraju, C. D.; Sanvito, S. Possible doping strategies for MoS 2 monolayers: An ab initio study. *Physical Review B* **2013**, *88*, 075420.

(9) Tan, A. M. Z.; Freysoldt, C.; Hennig, R. G. Stability of charged sulfur vacancies in 2D and bulk MoS 2 from plane-wave density functional theory with electrostatic corrections. *Physical Review Materials* **2020**, *4*, 064004.

(10) Zheng, H.; Yang, B.; Wang, D.; Han, R.; Du, X.; Yan, Y. Tuning magnetism of monolayer MoS2 by doping vacancy and applying strain. *Applied Physics Letters* **2014**, *104*.